# Engineering of two-photon spatial quantum correlations behind a double slit

W. H. Peeters, J. J. Renema, and M. P. van Exter
*Leiden Institute of Physics, Leiden University, P.O. Box 9504, 2300 RA Leiden, The Netherlands*
(Received 23 December 2008; revised manuscript received 18 February 2009; published 16 April 2009)

This paper demonstrates the engineering of spatially entangled two-photon states behind a double slit by tailoring the incident pure two-photon state. We experimentally characterize many different two-photon states by measuring their complete two-photon interference patterns in the far field of the double slit. Spatial entanglement right behind the double slit can reside in either the modulus or the phase of the two-photon field. The balance between these two types of entanglement is fully controlled by experimentally utilizing the phase-front curvatures of the pump beam and the phase-matching profile. We project either a far-field image or a magnified near-field image of the two-photon source onto the double slit. Our theoretical analysis shows how the two-photon interference pattern behind the double slit effectively acts as a phase-sensitive probe of the incident two-photon field profile. We thus present phase-sensitive measurements of the generated two-photon field profile probed in an image plane of the two-photon source.

DOI: 10.1103/PhysRevA.79.043817 PACS number(s): 42.50.Dv, 42.25.Hz, 03.67.Bg

## I. INTRODUCTION

Two photons are spatially entangled if their spatial degrees of freedom, residing in the phase space of transverse position and transverse momentum, are quantum correlated. This form of entanglement can be easily generated via the nonlinear process of spontaneous parametric down-conversion (SPDC), where a single pump photon splits into a pair of down-converted photons [1,2]. Spatial quantum correlations between two photons have played a pivotal role in many landmark experiments on fourth-order spatial interference [3,4], ghost imaging and ghost interference [1,5–7], quantum lithography [8,9], and orbital angular-momentum entanglement [10,11]. Other experiments have addressed wave-particle complementarity [12,13] and duality of one-photon and two-photon interferences [13–16]. Identification of spatial entanglement has been demonstrated via combined position-momentum measurements [17,18] and a recent violation of Bell inequalities [19,20].

Spatial entanglement created via SPDC is of a high-dimensional form, and the spatial Schmidt modes are generally quite complicated [21]. This spatial structure becomes less complicated by projecting each photon onto an array of holes. Behind a double slit, for example, the spatial entanglement exists between two transmitted photons of which each photon resides in a two-dimensional Hilbert space spanned by the upper slit and lower slit modes. Two-photon transmission through a double slit has been demonstrated with both indistinguishable [13,16] and distinguishable photons [9,12,14,22–28]. Extensions to high-dimensional forms of entanglement have been realized by using multislit apertures [29–32]. Methods for characterizing spatial entanglement behind a double slit have been demonstrated in Refs. [25,26,28].

To set the stage for further discussion, we restrict ourselves to double-slit illumination schemes that obey mirror symmetry with respect to the optical axis. The transmitted two-photon state then takes the form

$$|\Psi_{2\mathrm{ph}}\rangle = \cos(\alpha/2)\left(\frac{|\uparrow\downarrow\rangle + |\downarrow\uparrow\rangle}{\sqrt{2}}\right) + e^{i\varphi}\sin(\alpha/2)\left(\frac{|\uparrow\uparrow\rangle + |\downarrow\downarrow\rangle}{\sqrt{2}}\right), \quad (1)$$

where $|\uparrow\rangle$ and $|\downarrow\rangle$ represent transmissions through the upper slit and lower slit, respectively, and where $\alpha$ and $\varphi$ represent the state parameters. In principle, the above expression covers a large variety of two-photon spatial quantum correlations behind a double slit.

Experiments so far have addressed only a subclass of all two-photon states represented by Eq. (1). In many papers [12–14,16,22,23,26,28–32], the double slit is positioned far away from the two-photon source where transmission is dominated by photons emerging from opposite slits so that $0 \leq \alpha \leq \frac{1}{2}\pi$. Some of these papers have demonstrated how to control $\alpha$ within this range [13,14,26,32]. The opposite case, where both photons emerge from the same slit and $\alpha = \pi$, has been realized by positioning the double slit very close to the two-photon source [9,27]. This two-photon state plays a central role in the field of quantum lithography [8]. Until now, parameter $\alpha$ has not been tuned within the range $\frac{1}{2}\pi \leq \alpha \leq \pi$. No attention has been paid to the experimental tuning of $\varphi$ either, and most experiments seem to operate at $\varphi \approx 0$. Yet, it is known that $\varphi$ is highly relevant for the degree and type of spatial entanglement behind the double slit [26]. One could, for example, consider a maximally entangled state at $\alpha = \varphi = \frac{1}{2}\pi$ where the entanglement resides in the phase rather than the modulus of the two-photon field right behind the double slit [33].

In this paper we demonstrate full control over the state parameters $\alpha$ and $\varphi$. We achieve this by tailoring the imaging system in between the two-photon source and a single double slit. We switch between two imaging schemes: the crystal imaging scheme and the far-field (ff) imaging scheme. The crystal imaging scheme images (a plane close to) the two-photon source onto the double slit. We will call $\varphi$ the *curvature phase* because we control this phase by utilizing the

 

phase-front curvatures of both the phase-matching profile and the pump beam profile. We characterize more than 30 different two-photon states by measuring their complete two-photon interference patterns in the far field of the double slit. Our theoretical analysis provides a direct connection between the incident two-photon field profile and the state parameters $\alpha$ and $\varphi$. We show that the two-photon interference pattern behind the double slit effectively acts as a phase-sensitive probe of the incident two-photon field profile.

In our experiments, we use frequency degenerate SPDC in a periodically poled crystal where the signal and idler photons have the same polarization (type-I SPDC). Hence, the obtained spatial quantum correlations exist between indistinguishable photons. Our theoretical analysis, however, also applies to type-I SPDC in a uniform crystal and type-II SPDC in a periodically poled crystal. The analysis in this paper can thus also be used to engineer spatial quantum correlations between distinguishable photons.

The paper is organized as follows. The first theoretical part in Sec. II describes how to engineer two-photon spatial quantum correlations behind the double slit. We describe how parameters $\alpha$ and $\varphi$ depend on the incident two-photon field for the far-field and crystal imaging schemes. The second theoretical part in Sec. III describes one-photon and two-photon interferences behind the double slit. Section IV describes the experimental apparatus. The experimental results can be found in Sec. V. The tuning of the two-photon state is illustrated with a number of measured two-photon interference patterns. The observed one-photon and two-photon interference patterns are compared with theory. The paper ends with a concluding section and a discussion on the possibility to tune two-photon spatial quantum correlations in a higher-dimensional Hilbert space. The Appendix discusses the validity of our engineering model for various types of phase matching.

## II. THEORY: TWO-PHOTON STATE ENGINEERING

### A. Electromagnetic field behind double slit

The electromagnetic field behind a double slit is considered. We assume the field to be the response to an incident quasimonochromatic two-photon field in a pure state. Transmission through the double slit can happen in three ways: either both photons come through, one photon comes through and the other one is blocked, or both photons are blocked. The density matrix of the electromagnetic field behind the double slit can thus be written as

$$\hat{\rho}_{\text{out}} = P_0|\text{vac}\rangle\langle\text{vac}| + P_1\hat{\rho}_{1\text{p}} + P_2|\Psi_{2\text{ph}}\rangle\langle\Psi_{2\text{ph}}|, \tag{2}$$

where the first term represents vacuum, the second term represents a mixed one-photon field (one photon blocked), and the third term represents a pure two-photon field (both photons transmitted). Equation (2) emphasizes that experiments involving a single detector depend on both the one-photon component and the two-photon component.

We now direct our attention to the two-photon part $|\Psi_{2\text{ph}}\rangle$ of the transmitted state. Each photon can pass the double slit through either the upper or lower slit. We will denote these two spatial modes by $|\uparrow\rangle$ and $|\downarrow\rangle$, respectively. The most general form of the two-photon part of the transmitted state can thus be written as

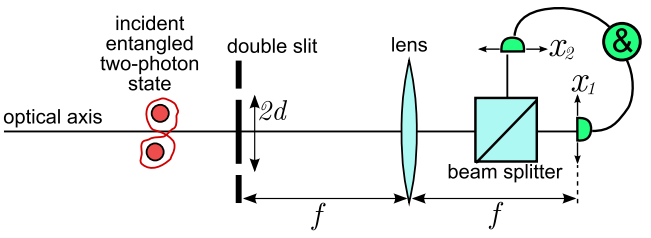


FIG. 1. (Color online) Detection part of the double-slit setup supporting the theoretical framework in Secs. II and III.

$$|\Psi_{2\text{ph}}\rangle = c_1|\uparrow\uparrow\rangle + c_2|\uparrow\downarrow\rangle + c_3|\downarrow\uparrow\rangle + c_4|\downarrow\downarrow\rangle, \tag{3}$$

where the two Hilbert spaces belong to the two photons. We will now restrict ourselves to illumination setups that obey mirror symmetry with respect to the optical axis (see Fig. 1). This symmetry implies that $c_1=c_4$ and $c_2=c_3$ so that reversal of all arrows leaves the quantum state unaltered. With this restriction, the most general form of the two-photon state becomes

$$|\Psi_{2\text{ph}}\rangle = \cos(\alpha/2)\left(\frac{|\uparrow\downarrow\rangle + |\downarrow\uparrow\rangle}{\sqrt{2}}\right) + e^{i\varphi}\sin(\alpha/2)\left(\frac{|\uparrow\uparrow\rangle + |\downarrow\downarrow\rangle}{\sqrt{2}}\right), \tag{4}$$

being a coherent superposition of two states that we will denote as *antipaired* and *paired*. In the antipaired state the two photons emerge from opposite slits. In the paired state the photons stick together and emerge from the same slit, being either the upper slit or the lower slit. Figure 2 shows how the two-photon state can be depicted as a point on a two-particle Bloch sphere. We call $\varphi$ the curvature phase because it depends on the phase-front curvature of the incident two-photon field (details in Secs. II B–II E).

The quantum state in Eq. (4) represents a spatially entangled qubit pair, where the quantum information of each photonic qubit is encoded in its spatial properties. The degree of entanglement within a qubit pair is often quantified via the concurrence [34,35]. For our case, the concurrence becomes [26]

$$C = \sqrt{1 - \sin^2(\alpha)\cos^2(\varphi)}. \tag{5}$$

On the two-qubit Bloch sphere of Fig. 2, the concurrence equals the distance from the point on the sphere to the vertical axis of the sphere. Quantum states on the horizontal equator ($\varphi = \pm\pi/2$) are maximally entangled regardless the value of $\alpha$. Quite remarkably, until now, hardly any attention has been paid to the experimental tuning of $\varphi$. This paper describes how to tune both $\alpha$ and $\varphi$.

In our experiments, the two photons are not distinguishable by their energy or polarization. Probabilistic separation is achieved with a beam splitter behind the double slit (see Fig. 1). The spatial quantum correlations are detected after postselection on simultaneous clicks of two detectors in the

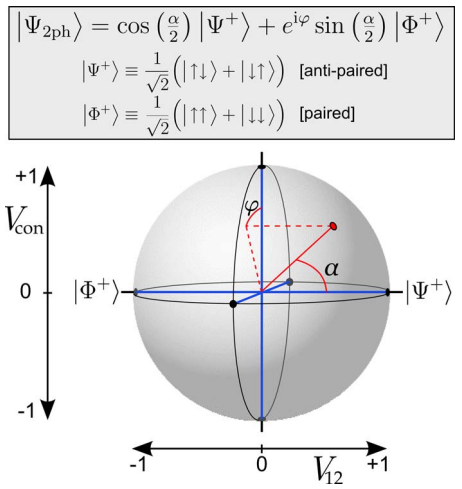


FIG. 2. (Color online) Bloch-sphere representation of a two-qubit state $|\Psi_{2ph}\rangle$ that is restricted to the two-dimensional expression shown above. The states $|\Phi^+\rangle$ and $|\Psi^+\rangle$ are two of the four maximally entangled Bell states. The indicated two-photon visibilities $V_{12}=\cos(\alpha)$ and $V_{con}=\sin(\alpha)\cos(\varphi)$ directly relate to the position on the sphere. The concurrence of $|\Psi_{2ph}\rangle$ is given by $C=\sqrt{1-V_{con}^2}$. The two-qubit state is thus maximally entangled on the horizontal equator.

output ports of the beam splitter. The events in which the photons are reflected or transmitted in pairs are discarded. The experiments could fairly easily be extended to distinguishable spatially entangled photons by using type-II SPDC in a periodically poled crystal (see Sec. II C).

### B. Quantum state engineering

The main point of this paper is to demonstrate full control over the two-photon state behind the double slit as given by Eq. (4). We thus need to describe how $\alpha$ and $\varphi$ depend on the incident quasimonochomatic pure two-photon state $|\Psi_{in}\rangle$. The incident state is fully characterized by the two-photon field profile in the double-slit plane,

$$A_{slits}(x_1,x_2) \equiv \langle vac|\hat{E}^{(+)}_{slits}(x_1)\hat{E}^{(+)}_{slits}(x_2)|\Psi_{in}\rangle. \quad (6)$$

The operator $\hat{E}^{(+)}_{slits}(x)$ is the positive frequency electric field operator at transverse position $x$ in the double-slit plane. The two-photon field profile can be interpreted as the complex probability amplitude for simultaneous detection of one photon at position $x_1$ and the other photon at transverse position $x_2$.

The two-photon field profile behind the double slit is just the sampled version of the incident two-photon field profile. We now assume that the slits are narrower than any spatial structure of the incident two-photon field profile. The transmitted two-photon state is then fully characterized by four complex amplitudes $A_{slits}(\pm d,\pm d)$, where $2d$ is the slit separation. Because of the assumed mirror symmetry with respect to the optical axis we have $A_{slits}(d,d)=A_{slits}(-d,-d)$ and $A_{slits}(d,-d)=A_{slits}(-d,d)$. The first pair of two-photon amplitudes corresponds to paired photons, and the latter pair corresponds to antipaired photons. The coefficients of the transmitted two-photon state in Eq. (4) can thus be associated with the incident two-photon field profile via

$$p \equiv e^{i\varphi}\tan\left(\frac{\alpha}{2}\right) = \frac{A_{slits}(d,d)}{A_{slits}(d,-d)}. \quad (7)$$

Here, we have defined $p$ as the *engineering parameter*, which fully determines the transmitted two-photon state. Equation (7) plays a central role in this paper because it describes the relationship between the incident two-photon field profile and the two-photon state behind the double slit.

### C. Incident two-photon state

In this section we calculate the incident two-photon field profile for a two-photon state produced via the nonlinear process of SPDC. We consider frequency degenerate SPDC in the low-conversion regime with cw pumping along the positive $z$ direction. The nonlinear crystal has two parallel planar facets in transverse $xy$ planes separated by length $L$. We assume the divergence of the pump beam to be small such that the Rayleigh range is much larger than the crystal length. The pump photon has energy $\hbar\omega_p$, and the signal and idler photons individually have approximately energy $\hbar\omega_0=\frac{1}{2}\hbar\omega_p$.

The phase-matching condition is essential for the precise form of the generated two-photon field profile. All equations derived below are based on noncritical type-I phase matching. Noncritical phase matching is generally applied in periodically poled crystals, and it means that the pump beam is orientated along a principal axis of the crystal. However, in the Appendix we show that our analysis also applies to noncritical type-II as well as critical type-I phase matching. In the latter case, the transverse walk-off distance of the pump should be much smaller than the pump beam diameter, which can be achieved by sufficiently loose focusing of the pump.

The first step toward quantum state engineering is to calculate the two-photon field profile in the crystal-center plane. Following Ref. [36], we write for the momentum representation of this two-photon field profile

$$\tilde{A}_{crys}(\mathbf{q}_1,\mathbf{q}_2) \propto \tilde{E}_p(\mathbf{q}_1+\mathbf{q}_2)\tilde{\xi}(\mathbf{q}_1-\mathbf{q}_2), \quad (8)$$

where the tilde symbol indicates the spatial Fourier transform, $\tilde{E}_p(\mathbf{q})$ is the momentum representation of the pump profile in the crystal-center plane, and $\mathbf{q}_{1,2}$ are the transverse wave vectors of the two photons. The phase-matching profile is

$$\tilde{\xi}(\Delta\mathbf{q}) = \mathrm{sinc}\left(\phi_0 + \frac{L|\Delta\mathbf{q}|^2}{8n_0\omega_0/c}\right), \quad (9)$$

where $\mathrm{sinc}(x)\equiv\sin(x)/x$, $L$ is the crystal length, and $n_0$ is the refractive index at the down-converted frequency. The $\phi_0$ term accounts for the phase mismatch in forward direction.

The second step is to calculate the propagation from the crystal toward the double slit. The propagation of the two-photon field profile is described via

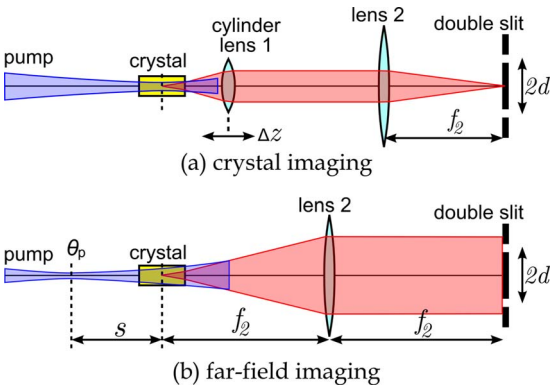


FIG. 3. (Color online) Two schemes for quantum state engineering. (a) Crystal imaging: a plane inside or close to the crystal is imaged onto the double slit. The two engineering parameters are the magnification $M \equiv f_2/f_1$ and the longitudinal position $\Delta z$ of lens 1. The illustration shows $\Delta z=0$, where the front focal plane of lens 1 coincides with the crystal center. (b) Far-field imaging: the far field of the crystal, which is pumped by a Gaussian beam, is imaged onto the double slit. The two engineering parameters are the pump divergence $\theta_p$ and longitudinal position of the pump waist $s$.

$$A_{\text{slits}}(\mathbf{x}_1,\mathbf{x}_2) = \int\int A_{\text{crys}}(\mathbf{x}',\mathbf{x}'')h(\mathbf{x}_1,\mathbf{x}')h(\mathbf{x}_2,\mathbf{x}'')d\mathbf{x}'\,d\mathbf{x}'', \tag{10}$$

where $h(\mathbf{x},\mathbf{x}')$ is the (classical) electric field propagator [37] from the crystal to the double slit at radial frequency $\omega_0$. The two-photon field profile remains factorized after propagation through any paraxial *ABCD* lens system. Therefore, it is convenient to think of the pump profile and the phase-matching profile as two separately propagating profiles. The two-photon field profile at any position $z$ along the optical axis can thus be written as

$$A(\mathbf{x}_1,\mathbf{x}_2;z) \propto E_{p,z}\left(\frac{\mathbf{x}_1+\mathbf{x}_2}{2};z\right)\xi_z\left(\frac{\mathbf{x}_1-\mathbf{x}_2}{2};z\right), \tag{11}$$

where $E_{p,z}(\mathbf{x};z)$ is the pump beam, $\xi_z(\mathbf{x};0)\equiv\xi(\mathbf{x})$, and $\xi_z(\mathbf{x};z)$ is the phase-matching profile propagated at radial frequency $\omega_p$ from the crystal center to position $z$.

In the final step, we calculate the engineering parameter $p$ from Eq. (7). This calculation requires a one-dimensional description of the incident two-photon field profile. Below, we argue why it is allowed to single out one transverse dimension in Eq. (11) for the imaging schemes that we use. It may, however, not be concluded that a one-dimensional treatment is permitted for any general imaging scheme. The problem is that the phase-matching profile $\xi_z(\mathbf{x};z)$ does not factorize in two functions for the two transverse dimensions. The pump beam $E_{p,z}(\mathbf{x};z)$, which we will assume to have a Gaussian profile, nicely factorizes in the two transverse directions.

In the far-field imaging scheme [see Fig. 3(b)], the slit separations that we use are much smaller than the phase-matching profile. The phase-matching profile is thus approximately constant in the region of the slits, and the two-photon field scales with the pump profile. Singling out one dimension is thus allowed for the far-field imaging scheme.

Our crystal imaging scheme [see Fig. 3(a)] is based on a mixed form of imaging, where lens 1 is a cylinder lens and lens 2 is a standard lens. This mixed form of imaging produces only a crystal image in the direction perpendicular to the slits ($x$ direction), while it retains the far-field image in the direction parallel to the slits ($y$ direction). The size of the phase-matching profile along the $x$ direction is now similar to the slit separation, whereas the profile is much more extensive along the $y$ direction. Furthermore, detection occurs via projection on round detection modes that are much smaller than the phase-matching profile along $y$ direction in the double-slit plane (2.1 mm versus 9.2 mm full width at half maximum intensity). The incident two-photon field profile is thus probed only around $q_y \simeq 0$, and singling out the $x$ dimension is allowed.

### D. Crystal imaging scheme

Our crystal imaging scheme can produce any two-photon state on the left hemisphere of the two-qubit Bloch sphere (see Fig. 2). The working principle is that the crystal is imaged onto the double slit. For collinear phase matching ($|\phi_0| \ll \pi$), the two photons leave the crystal from approximately the same transverse position, and they arrive in the same way at the double slit [38]. Hence, the two-photon state behind the double slit is dominated by the paired contribution.

The crystal imaging scheme is shown in Fig. 3(a). The pump beam is weakly focused in the crystal-center plane. A plane close to the crystal center, i.e., within the Rayleigh range of the pump beam, is imaged onto the double slit with two lenses. The double slit is positioned in the back focal plane of the second lens; the corresponding object plane then coincides with the front focal plane of the first lens. The precise position of the object plane can now be tuned by moving the first lens longitudinally. We call this displacement the defocus distance $\Delta z$, where $\Delta z=0$ if the object plane coincides with the crystal-center plane, and $\Delta z>0$ for an increased distance between lens and crystal. The magnification of the imaging system is $M \equiv f_2/f_1$, where $f_1$ and $f_2$ are the focal lengths of the first and the second lens, respectively. The slit separation is $2d$.

The profile at the double slit is just the magnified version of the two-photon field profile in the object plane. The engineering parameter $p$, which completely determines the two-photon state behind the double slit via Eq. (7), becomes

$$p = \frac{A\left(\frac{+d}{M},\frac{+d}{M};\Delta z\right)}{A\left(\frac{+d}{M},\frac{-d}{M};\Delta z\right)}, \tag{12}$$

where $A(x_1,x_2;z)$ is the two-photon field profile of Eq. (11). Note that the object plane inside the crystal has actually moved over a distance $n_0\Delta z$. For convenience, we have used the propagation length $\Delta z$ instead of $n_0\Delta z$. This choice implies that $A(x_1,x_2;z)$ must be treated as a two-photon field

profile that has propagated over a distance $z$ through an imaginary medium with refractive index $n=1$.

It is important to realize that the phase-matching profile $\xi_z(x;\Delta z)$ is much narrower than the pump profile $E_{p,z}(x;\Delta z)$. As a consequence, $d/M$ is much smaller than the waist of the pump beam in the relevant range of operation. Therefore, we can approximate the engineering parameter via

$$p=\frac{E_{p,z}\left(\frac{d}{M};\Delta z\right)\xi_z(0;\Delta z)}{E_{p,z}(0;\Delta z)\xi_z\left(\frac{d}{M};\Delta z\right)}\approx\frac{\xi_z(0;\Delta z)}{\xi_z\left(\frac{d}{M};\Delta z\right)}. \tag{13}$$

The argument and the absolute value of $p$ are determined by the phase-front curvature of $\xi_z(x;\Delta z)$ and amplitude variations of $\xi_z(x;\Delta z)$, respectively.

By using the expression for the phase-matching profile in Eq. (9), we find the explicit expression

$$p=\frac{\int \mathrm{sinc}(\phi_0+x^2)\exp(-ibx^2)dx}{\int \mathrm{sinc}(\phi_0+x^2)\exp(-ibx^2-iax)dx}, \tag{14}$$

where $\mathrm{sinc}(x)\equiv\sin(x)/x$ and $\phi_0$ is the phase mismatch. The dimensionless parameters

$$a\equiv\frac{2d}{M\sqrt{Lc/(n_0\omega_p)}}, \tag{15}$$

$$b\equiv\frac{\Delta z}{L/(2n_0)}, \tag{16}$$

are the scaled slit separation and the scaled defocus distance, respectively. The two-photon state behind the double slit can be engineered by tailoring parameters $a$ and $b$. Unfortunately, there is no simple analytic expression for the integrals in Eq. (14).

We can gain physical intuition for the influence of $a$ and $b$ on parameter $p$ by considering two general properties of the phase-matching profile $\xi_z(x;z)$. First, the phase front of $\xi_z(x;z)$ is flat at the crystal center. This flatness causes parameter $p$ to be real valued for $\Delta z=0$ making the curvature phase $\varphi=0$. Second, $|p|>1$ at any $\Delta z$, as the maximum of $\xi_z(x;z)$ stays at the optical axis during propagation. Numerical evaluations show that 98% of the left hemisphere of the two-qubit Bloch sphere is covered by varying $a\in[0,8]$ and $b\in[-6,6]$. These evaluations also show that the coverage can be brought arbitrarily close to 100% for larger ranges of $a$ and $b$.

### E. Far-field imaging scheme

Our far-field imaging scheme can produce any two-photon state on the right-hand hemisphere of the two-qubit Bloch sphere (see Fig. 2). The working principle is that the far field of the crystal is imaged onto the double slit. The photons propagate with approximate opposite transverse momenta, so the photons arrive at approximate opposite transverse positions in the double-slit plane. Hence, the two-photon state behind the double slit is dominated by the antipaired contribution.

The far-field imaging scheme is shown in Fig. 3(b). The crystal is pumped with a weakly focused Gaussian beam with divergence $\theta_p$ defined via $\tilde{E}_p(\theta\omega_p/c)\propto\exp(-\theta^2/\theta_p^2)$. The waist of the pump beam lies at a distance $s$ in front of the crystal center. The far field of the crystal is symmetrically imaged onto the double slit by a lens with focal length $f_2$. The slit separation is $2d$.

It is important to realize that the far-field pump profile $\tilde{E}_p(q)$ is much narrower than the far-field phase-matching profile $\tilde{\xi}(q)$. As a consequence, $d/f_2$ is much smaller than the divergence of the phase-matching profile in the relevant range of operation. Therefore, the engineering parameter $p$ can be approximated via

$$p=\frac{\tilde{E}_p\left(\frac{d\omega_p}{f_2c}\right)\tilde{\xi}(0)}{\tilde{E}_p(0)\tilde{\xi}\left(\frac{d\omega_p}{f_2c}\right)}\approx\frac{\tilde{E}_p\left(\frac{d\omega_p}{f_2c}\right)}{\tilde{E}_p(0)}, \tag{17}$$

where the first equality is found by combining Eqs. (7), (8), and (10).

Insertion of the described pump profile yields the explicit expression

$$p=\exp\left[-\left(\frac{d}{f_2\theta_p}\right)^2\left(1+\frac{is}{z_R}\right)\right], \tag{18}$$

where $z_R\equiv 2c/(\theta_p^2\omega_p)$ is the Rayleigh range of the pump beam. From this expression it is clear that any two-photon state with $|p|<1$ can be produced by tailoring the divergence of the pump beam $\theta_p$ and its waist location $s$. These two-photon states lie on the right-hand hemisphere of the two-qubit Bloch sphere in Fig. 2.

## III. THEORY: INTERFERENCE BEHIND THE DOUBLE SLIT

### A. State determination by two-photon interference

This section describes how we analyze the engineered two-photon state. We show that the two-photon interference pattern in the far field of the double slit serves as a fingerprint of the quantum state described by Eq. (4). Figure 1 shows the geometry of the detection setup. The far field of the double slit is formed in the back focal plane of a lens with focal length $f$. The two photons are probabilistically separated by a beam splitter (see Sec. II A). Two detectors are positioned in the far-field planes formed in the two output ports of the beam splitter.

In the limit of narrow slits, the coincidence count rate in the far field of the double slit becomes [26]

$$R_{cc}(x_1,x_2)\propto 1+V_{\mathrm{diff}}\cos(\phi_1-\phi_2)+V_{\mathrm{sum}}\cos(\phi_1+\phi_2)+V_{\mathrm{con}}[\cos(\phi_1)+\cos(\phi_2)], \tag{19}$$

where the interslit phase differences $\phi_i$ relate to the detector positions $x_i$ via $\phi_i=2d\omega_0x_i/fc$, where $2d$ is the slit separation

and $\hbar\omega_0$ is the energy of each photon. The coefficients are given by

$$V_{\mathrm{diff}} = \cos^2(\alpha/2), \tag{20}$$

$$V_{\mathrm{sum}} = \sin^2(\alpha/2), \tag{21}$$

$$V_{\mathrm{con}} = \sin(\alpha)\cos(\varphi), \tag{22}$$

where we call $V_{\mathrm{sum}}$ the visibility in the sum of coordinates and $V_{\mathrm{diff}}$ the visibility in the difference of coordinates. Coefficient $V_{\mathrm{con}}$ relates to the fringe pattern in the single count rate conditioned on transmission of the second photon through the double slit. Therefore, we call $V_{\mathrm{con}}$ the *conditional one-photon visibility*. Note that $V_{\mathrm{con}}$ is allowed to become negative and that this sign has a clear and measurable physical meaning. It is just for convenience that we incorporate the sign of $\sin(\alpha)\cos(\varphi)$ in what we call the conditional one-photon visibility.

The visibilities in the sum and difference of coordinates obey $V_{\mathrm{diff}}+V_{\mathrm{sum}}=1$. It is convenient to remove this redundancy and use only one quantity. Therefore, we define

$$V_{12} \equiv V_{\mathrm{diff}} - V_{\mathrm{sum}} = \cos(\alpha) \tag{23}$$

as the *two-photon visibility difference*. The interference pattern of Eq. (19) is now determined by just two quantities being $V_{12}$ and $V_{\mathrm{con}}$.

The far-field two-photon interference pattern serves as a fingerprint of the two-qubit state. State parameter $\alpha$ is determined by $V_{12}=\cos(\alpha)$ and state parameter $|\varphi|$ is then determined by $V_{\mathrm{con}}=\sin(\alpha)\cos(\varphi)$. The two-qubit Bloch sphere in Fig. 2 graphically connects these visibilities to the two-photon state: the in-plane horizontal coordinate is $V_{12}$ and the vertical coordinate is $V_{\mathrm{con}}$. The sign of $\varphi$, indicating whether the state is on the front or rear side of the sphere, cannot be determined from the two-photon interference pattern. This sign, however, has limited physical meaning as the two-photon interference pattern, anywhere behind the double slit, is invariant under sign reversal of $\varphi$.

The experimental visibilities can easily be expressed in terms of the engineering parameter $p$, which characterizes the two-photon state behind the double slit via Eq. (7). By combining Eqs. (7), (22), and (23), we find

$$V_{12} = \frac{1-|p|^2}{1+|p|^2}, \tag{24}$$

$$V_{\mathrm{con}} = \frac{p+p^*}{1+|p|^2}, \tag{25}$$

enabling us to explicitly predict the outcome of the experiments based on the calculated parameter $p$.

### B. Interpretation of the two-qubit Bloch sphere

The two-qubit Bloch sphere in Fig. 2 is a graphical representation of a pure two-qubit state that is restricted to the indicated linear superposition of two Bell states. All possible two-photon states on this sphere share a common Schmidt basis [26,39]. These Schmidt states are located on the north and south poles of the sphere, being $|\eta_+\rangle|\eta_+\rangle$ and $|\eta_-\rangle|\eta_-\rangle$, respectively, where $|\eta_\pm\rangle \equiv \frac{1}{\sqrt{2}}(|\uparrow\rangle \pm |\downarrow\rangle)$. The concurrence $C$ is thus directly related to the vertical coordinate $V_{\mathrm{con}}$ on the sphere. By combining Eqs. (5) and (22) we find [26]

$$C = \sqrt{1 - V_{\mathrm{con}}^2}. \tag{26}$$

The physical interpretation of Eq. (26) is simple. If the photon pair is strongly entangled ($C \simeq 1$), the spatial state of each individual photon is necessarily mixed and cannot produce a strong interference pattern on its own ($V_{\mathrm{con}} \simeq 0$). In the opposite case of an approximately nonentangled state ($C \simeq 0$), the state of each individual photon is almost pure and produces strong interference ($V_{\mathrm{con}} \simeq 1$).

The sphere provides a clear graphical interpretation of a well-known complementarity relation between $V_{12}$ and $V_{\mathrm{con}}$. By combining Eqs. (22) and (23) it is easily shown that [40,41]

$$V_{12}^2 + V_{\mathrm{con}}^2 \leq 1 \tag{27}$$

or $V_{12}^2 \leq C^2$. The stronger the entanglement, the larger $|V_{12}|$ is allowed to become. The absolute two-photon visibility difference $|V_{12}|$ determines the correlation strength of the transverse positions of the photons right behind the double slit. Absence of this type of correlation, however, does *not* imply absence of entanglement because the entanglement could also reside in the phase rather than the modules of the two-photon field profile [33]. Inequality (27) becomes an equality for two-photon states with zero curvature phase ($\varphi=0$).

The two-qubit Bloch sphere also suggests the existence of a third visibility,

$$V_p \equiv \sin(\alpha)\sin(\varphi) = \frac{-i(p-p^*)}{1+|p|^2}, \tag{28}$$

being the coordinate along the "out of paper" direction. Together with $V_{12}$ and $V_{\mathrm{con}}$, this third coordinate forms an exact complementarity relation

$$V_{12}^2 + V_p^2 = C^2. \tag{29}$$

In the fully entangled case, where $C=1$ and $V_{\mathrm{con}}=0$, a projective measurement on photon A provides all quantum information on photon B. The basis in which this quantum information is obtained depends on the character of the entanglement. At $V_{12}=\pm 1$ and $V_p=0$, a projection of photon A in the slit basis $|\uparrow\rangle, |\downarrow\rangle$ provides full "which path" information on photon B. At $V_{12}=0$ and $V_p=\pm 1$, photon A must be projected onto the states $|\uparrow\rangle \pm i|\downarrow\rangle$ to obtain which path information on photon B. It is yet unclear how to experimentally determine the third coordinate $V_p$.

### C. One-photon interference

We consider the pattern of the total intensity in the far field of a double slit that is illuminated with a pure two-photon state. The visibility of this fringe pattern is called the *unconditional one-photon visibility* $V_{\mathrm{unc}}$. The unconditional and conditional one-photon visibilities generally differ from each other because $V_{\mathrm{con}}$ solely depends on the two-photon component behind the double slit, whereas $V_{\mathrm{unc}}$ also depends

on the one-photon part. The electromagnetic field behind the double slit is often even dominated by the one-photon part, i.e., $P_1 > P_2$ in Eq. (2).

For symmetric double-slit illumination, the intensity profile in the far-field plane of the double slit (see Fig. 1) is of the form

$$I(x) \propto 1 + V_{\mathrm{unc}} \cos(\phi), \tag{30}$$

where the interslit phase difference $\phi$ relates to the detector position $x$ via $\phi = 2d\omega_0 x/fc$. Equation (30) implicitly defines the unconditional one-photon visibility $V_{\mathrm{unc}}$. The second-order correlation function at the slits determines $V_{\mathrm{unc}}$ via [42]

$$V_{\mathrm{unc}} = \frac{G^{(1)}(d,-d)}{G^{(1)}(d,d)}. \tag{31}$$

The outcome of this equation is real valued due to the assumed illumination symmetry of the setup. Like the conditional one-photon visibility, we have defined the unconditional one-photon visibility such that it can become negative.

To calculate $V_{\mathrm{unc}}$, we need the second-order correlation function in the plane of the double slit. The second-order correlation function in a transverse plane can be calculated via [43]

$$G^{(1)}(\mathbf{x}_1,\mathbf{x}_2;z) \propto \int A^*(\mathbf{x}_1,\mathbf{x};z)A(\mathbf{x}_2,\mathbf{x};z)d\mathbf{x}, \tag{32}$$

where $A(\mathbf{x}_1,\mathbf{x}_2;z) \equiv \langle \mathrm{vac}|\hat{E}^{(+)}(\mathbf{x}_1;z)\hat{E}^{(+)}(\mathbf{x}_2;z)|\Psi_{\mathrm{in}}\rangle$ is the two-photon field profile and $|\Psi_{\mathrm{in}}\rangle$ is a pure monochromatic two-photon state associated with light propagating along the optical axis. Equation (32) has a broader range of validity than an alternative method based on the Van Cittert-Zernike theorem [15]. The latter theorem can only be used beyond the Rayleigh range of the two-photon source, and the two-photon source should be sufficiently spatially incoherent. The validity of Eq. (32) is retained close to the two-photon source even for partially coherent (realistic) two-photon sources.

As a first case, we calculate $V_{\mathrm{unc}}$ for the crystal imaging scheme that is treated in Sec. II D and shown in Fig. 3(a). By combining the generated two-photon field in Eqs. (8) and (9), the propagation to the double slit [Eq. (10)], and the formulas for the unconditional one-photon visibility in Eqs. (31) and (32), we find

$$V_{\mathrm{unc,cr}} = \frac{\int \mathrm{sinc}^2(\phi_0 + x^2)\exp(iax)dx}{\int \mathrm{sinc}^2(\phi_0 + x^2)dx}, \tag{33}$$

where $\mathrm{sinc}(x) \equiv \sin(x)/x$ and $a$ is the (dimensionless) scaled slit separation defined in Eq. (15). Again, we have assumed the pump profile to be much wider than the phase-matching profile. Unfortunately, there is no simple analytic expression for the integrals in Eq. (33).

As a second case, we consider the far-field imaging scheme that is treated in Sec. II E and shown in Fig. 3(b). By combining Eqs. (8), (10), (31), and (32) we find

$$V_{\mathrm{unc,ff}} = \exp\left[-\frac{1}{2}\left(\frac{d}{f_2\theta_p}\right)^2\left(1 + \frac{s^2}{z_R^2}\right)\right], \tag{34}$$

where $2d$ is the slit separation, $\theta_p$ is the pump divergence, and $z_R \equiv 2c/(\theta_p^2\omega_p)$ is the Rayleigh range of the pump beam. Again, we have assumed the far-field phase-matching profile to be much wider than the far-field pump profile. For this far-field imaging case, Eq. (34) can also be obtained via the Van Cittert-Zernike theorem.

### D. Duality between unconditional one-photon interference and two-photon interference

The relationship between unconditional one-photon interference and (conditional) two-photon interference was studied earlier in Refs. [13–16]. Saleh *et al.* [15] theoretically pointed out that there exists a profound duality between the two phenomena if far-field imaging is applied. In this section, we show how this duality manifests itself in our model. We find new duality relations that apply to our far-field imaging scheme, and we point out that the precise form of the duality relations strongly depends on the applied imaging scheme.

We consider far-field imaging [see Fig. 3(b)] with a pump beam that is loosely focused in the crystal-center plane ($s=0$). For this specific imaging scheme we find that $p = V_{\mathrm{unc,ff}}^2$ by comparing engineering parameter $p$ in Eq. (18) with $V_{\mathrm{unc}}$ in Eq. (34). After converting $p$ into the two-photon visibilities via Eqs. (24) and (25), we directly find duality relations

$$V_{12} = \frac{1 - V_{\mathrm{unc,ff}}^4}{1 + V_{\mathrm{unc,ff}}^4}, \tag{35}$$

$$V_{\mathrm{con}} = \frac{2V_{\mathrm{unc,ff}}^2}{1 + V_{\mathrm{unc,ff}}^4}, \tag{36}$$

which strictly correspond to the specified imaging geometry. Equations (35) and (36) describe how the unconditional intensity pattern serves as a fingerprint of the two-photon state.

In other imaging geometries, the duality relations become generally different or might even be multivalued. For example, the duality between $V_{12}$ and $V_{\mathrm{unc,ff}}$ was reported differently in Eq. (3.16) in Ref. [15] because the authors assumed a top-hat-shaped flat pump profile inside the crystal instead of a Gaussian-shaped flat pump profile. As another example, no one-to-one duality relations exist for the crystal imaging scheme [see Fig. 3(a)]. If crystal imaging is applied, some values of $V_{\mathrm{unc}}$ individually correspond to multiple values of $V_{12}$ and $V_{\mathrm{con}}$ (see Fig. 6).

## IV. EXPERIMENTAL APPARATUS

### A. General information

A schematic representation of the experimental apparatus is shown in Fig. 4. This apparatus can implement the crystal imaging scheme as well as the far-field imaging scheme. The working principles of these two imaging schemes are ex-

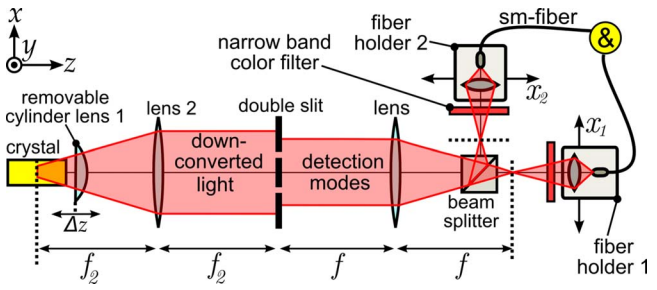


FIG. 4. (Color online) Schematic representation of the experimental apparatus. The down-converted light propagates from the crystal to the double slit via either the crystal imaging scheme (with cylinder lens) or the far-field imaging scheme (without cylinder lens). The longitudinal position of the cylinder lens can be adjusted. The two-photon interference pattern in the far field of the double slit is measured by scanning the fiber holders transversely. The two fiber holders are identical and consist of a single-mode (SM) fiber and an objective. The & symbol represents the detection of simultaneous photon arrivals.

plained in Secs. II D and II E. The technical details of the apparatus are given in Secs. IV B and IV C.

### B. Experimental apparatus in front of double slit

Photon pairs are generated via collinear spontaneous parametric down-conversion (SPDC) in a periodically poled $KTiOPO_4$ (PPKTP) crystal. The conversion is such that pump, signal, and idler waves have the same linear polarization. We pump the crystal with a continuous-wave $y$-polarized Gaussian beam propagating along the $z$ direction (laser: $Kr^+$, 200 mW at 413.1 nm). We operate in the quasimonochromatic limit by applying detection behind narrowband spectral filters ($\Delta\lambda=5$ nm at 826.2 nm). The crystallographic $x$ axis of the PPKTP is oriented along $z$ direction (pump direction) and the crystallographic $z$ axis is oriented along the $y$ direction (poling direction). The crystal is $L=5.09$ mm long, 1 mm thick in $y$ direction, and 2 mm wide in $x$ direction. The pump beam is absorbed behind the crystal by a GaP wafer that is antireflection coated for 826 nm.

It is important to know the phase mismatch $\phi_0$ because it strongly affects the engineering parameter $p$ in the crystal imaging scheme [see Eq. (14)]. For our 5-mm-long crystal, the temperature dependence of the phase mismatch is measured to be $\frac{\partial\phi_0}{\partial T}=1.059\ ^\circ\mathrm{C}^{-1}$ [44]. The phase-match temperature is found to be $T_0=(60.39\pm0.04)\ ^\circ\mathrm{C}$ from measurements of the temperature-dependent spectrum of the SPDC light in forward direction. All double-slit experiments are performed at a temperature $T=(60.70\pm0.01)\ ^\circ\mathrm{C}$ corresponding to a phase mismatch of $\phi_0=0.33\pm0.05$.

We illuminate the symmetric and centered double slit either with a centered far-field image of the source using an f-f imaging system (far-field imaging scheme) or a centered magnified image of the crystal by adding an extra cylinder lens (crystal imaging scheme). The double slit is positioned at 80 cm from the crystal center, and the fixed far-field imaging lens with focal length $f_2=(400\pm1)$ mm is positioned halfway. The removable cylinder lens with focal length $f_1$ produces a sharp image of the crystal-center plane only in the direction perpendicular to the slits; the cylinder lens leaves the imaging in the parallel direction unaffected. The cylinder lens can be moved further away from the crystal by an amount that we call the defocus distance $\Delta z$. The $y$-oriented slits are created by wire electrical discharge machining in a phosphor bronze plate.

Some size parameters of the experimental apparatus are adjustable in order to be able to engineer many different two-photon states behind the double slit. In the crystal imaging scheme, we adjust the slit separation $2d$, the focal length of the cylinder lens $f_1$, and the defocus distance $\Delta z$. In the far-field imaging scheme, we adjust the slit separation $2d$, the pump divergence $\theta_p$, and the distance from the pump waist to the crystal center $s$.

We have used six double-slit apertures with slit separations of $\{313,510,600,758,950,1400\}$ $\mu$m, all values with $\pm15$ $\mu$m uncertainty. The corresponding slit widths are $\{138,150,193,135,235,225\}$ $\mu$m. We used three different cylinder lenses with focal lengths of 12.7, 19.0, and 25.4 mm, all values with $\pm2\%$ uncertainty. The defocus distance is varied between $-0.20$ and 3.30 mm. The null position of $\Delta z$ corresponds to the point where the front focal plane coincides with the crystal center. This position is calibrated to a precision of $\pm0.04$ mm by reflecting a reference beam, which is backwardly focused in the primary focal plane of the cylinder lens on the front and rear crystal facets (reversed autocollimation). For the far-field imaging experiments with $s=0$, we used three different pump divergences, 0.73, 1.31, and 2.27 mrad, all values with 10% uncertainty. Some measurements have been performed with pump waists in front of the crystal such that $s\neq0$.

### C. Experimental apparatus behind double slit

The two photons behind the double slit are probabilistically separated with a beam splitter behind the double slit. The events where the photons are both reflected or both transmitted are discarded (see Sec. II A). A lens with focal length $f=400$ mm is positioned between the double slit and the beam splitter. The lens images the far field of the double slit onto two intermediate detection planes in the two output ports of the beam splitter.

Detection occurs via projection onto the mode profiles of two single-mode fibers. In the double-slit plane, the centered Gaussian detection modes have (loose) waist diameters of 2.1 mm for each mode (full widths at half maximum intensity). Correspondingly, the detection modes have waist diameters of 70 $\mu$m in the intermediate detection planes (full widths at half maximum intensity). The finite size of the detection modes does not affect the observed fringe visibility because the field projection is phase sensitive, and the period of the two-photon fringe pattern is at least 240 $\mu$m which is more than three times larger than the width of the detection modes. The two-photon interference pattern is measured by scanning two computer-controlled detection stages transversely. Each detection stage comprises the fiber tip and an objective with an effective focal length of 8 mm. The detection modes thus only move in the far field of the double slit,

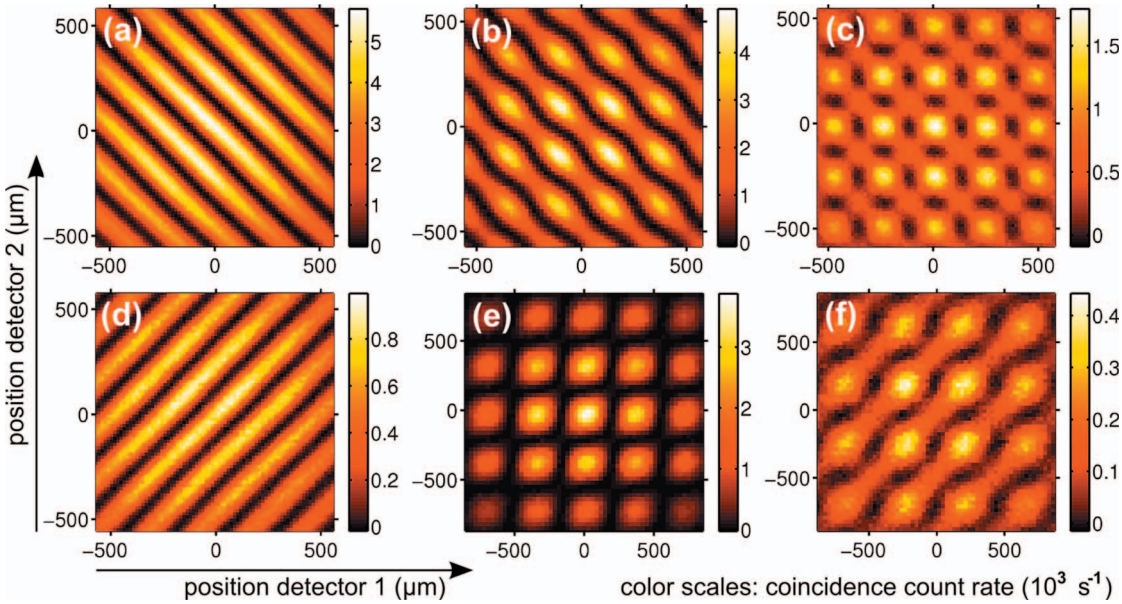


FIG. 5. (Color) Various measured two-photon interference patterns in the far field of a double slit. Measurements (a)–(c) are obtained with the crystal imaging scheme and (d)–(f) are obtained with the far-field imaging scheme. Measurements (c) and (f) have nonzero curvature phase. The slit separation is 1.40 mm for measurements (a)–(d), 0.95 mm for measurement (e), and 0.76 mm for measurement (f). The indicated coincidence count rates have been corrected for accidental coincidences.

while their intensity profiles remain fixed in the double-slit plane.

The single-mode fibers are coupled to single-photon counting modules (Perkin-Elmer SPCM-AQR-14-FC). Simultaneous photon detections are registered by coincidence electronics. The applied gate time of our pulse correlator is $\tau_g = (1.73 \pm 0.01)$ ns. If two photons from *different* photon pairs are detected within this time window, it is fallaciously registered as a coincidence count. The count rate of these so-called *accidental* counts is

$$R_{\mathrm{ac}} = R_1 R_2 \tau_g, \tag{37}$$

where $R_1$ and $R_2$ are the raw single count rates in detector 1 and detector 2, respectively. The "real" coincidence count rate is obtained by subtracting the accidental count rate from the measured coincidence count rate. In our experiments, the accidental count rate typically accounts for about 10%–45% of the rawly measured coincidence count rate. The photon count integration time is 1 s for each pixel of the measured two-photon interference patterns.

## V. EXPERIMENTAL RESULTS

### A. General information

In this section we demonstrate the engineering of many different two-photon states behind the double slit. Each two-photon state is characterized via a measurement of the two-photon interference pattern in the far field of the double slit. The interference patterns provide the conditional one-photon visibility $V_{\mathrm{con}}$ and the two-photon visibility difference $V_{12}$ for each two-photon state. The manner in which these visibilities relate to the engineered two-photon state is graphically indicated on the two-qubit Bloch sphere in Fig. 2. The intensity fringe patterns are also recorded. These yield the unconditional one-photon visibility $V_{\mathrm{unc}}$. The analysis and tuning of the two-photon interference pattern are discussed in Sec. V B. Quantitative comparison with theory is performed in Secs. V C–V F.

### B. Analysis and tuning of two-photon interference patterns

Six examples of measured two-photon interference patters are shown in Figs. 5(a)–5(f). This selection covers a whole range of different double-slit imaging types. The upper row is measured with the crystal imaging scheme, and the lower row is measured with the far-field imaging scheme. The left column contains the two extreme cases where the slit separation is large compared to the coherence width of the down-converted light at the double slit. The central column is measured with slit separations similar to the coherence width. The right-hand column is measured with a certain amount of defocusing, meaning that either $\Delta z \neq 0$ for the crystal imaging scheme or $s \neq 0$ for the far-field imaging scheme.

The general form of the two-photon interference pattern, given by Eq. (19), allows for an insightful interpretation of the fringe visibilities. The three visibilities—$V_{\mathrm{sum}}$, $V_{\mathrm{diff}}$, and $V_{\mathrm{con}}$—become isolated after projections on the +45° diagonal, the −45° diagonal, and the horizontal axis, respectively. Mathematically, these projections result in

$$R_{+45^\circ}(x_1 + x_2) \propto 1 + V_{\mathrm{sum}} \cos\left(\frac{x_1 + x_2}{x_s/2\pi}\right), \tag{38}$$

$$R_{-45^\circ}(x_1 - x_2) \propto 1 + V_{\mathrm{diff}} \cos\left(\frac{x_1 - x_2}{x_s/2\pi}\right), \tag{39}$$

$$R_{0^\circ}(x_1) \propto 1 + V_{\mathrm{con}} \cos\left(\frac{x_1}{x_s/2\pi}\right), \tag{40}$$

where $x_s$ is the fringe period for coherent light at the down-converted wavelength. In order not to deform the projection, it is important to select an integer number of fringe periods in the direction orthogonal to the projection axis. Each fringe pattern has been analyzed by fitting these three projections after including the effect of limited angular diffraction due to the finite slit width [26]. The two-photon visibility difference is then found via its definition $V_{12} \equiv V_{\mathrm{diff}} - V_{\mathrm{sum}}$. The sum $V_{\mathrm{diff}} + V_{\mathrm{sum}} = 1$ is automatically obeyed if the experimental apparatus is aligned properly.

In the far-field imaging scheme, the two photons arrive at approximately opposite positions in the double-slit plane. Hence, two-photon transmission is dominated by the antipaired two-photon component causing $V_{12}$ to be positive. One quickly recognizes that the lower three interference patterns have positive $V_{12}$ because the fringes projected on the $-45°$ diagonal are more distinct than the fringes projected on the $+45°$ diagonal. The extreme case, where the slit separation is large compared to the pump divergence, is shown in Fig. 5(d). This two-photon state is almost completely antipaired as we find $V_{12} = (96 \pm 1)\%$. Paired two-photon transmission can be increased by increasing the pump divergence relative to the slit separation. Such an increase has been applied to situation (e) where the fringe orientation is hardly visible and $V_{12} = (25 \pm 3)\%$.

The tuning of $V_{12}$ in the crystal imaging scheme is analogous. The photons arrive at approximately equal positions in the double-slit plane. Hence, two-photon transmission is dominated by the paired two-photon amplitude, causing $V_{12}$ to be negative. The extreme case is shown in Fig. 5(a), where the slit separation is large compared to the size of the magnified phase-matching profile. The corresponding two-photon state is almost completely paired and we determine $V_{12} = -(96 \pm 1)\%$. The antipaired two-photon transmission can be enhanced by increasing the magnification of the imaging system or reducing the slit separation. In situation (b), the slit separation is reduced to about the size of the magnified phase-matching profile $\xi_z(\frac{x}{M}; \Delta z = 0)$ resulting in $V_{12} = -(89 \pm 1)\%$.

The conditional one-photon visibility can be interpreted as the fringe visibility produced by each individual photon of the transmitted pair. By projecting the two-photon fringe pattern on the horizontal axis, it is easily recognized that patterns (a) and (d) have $V_{\mathrm{con}} \approx 0$. The conditional one-photon visibility is close to 100% for pattern (e). Patterns (b) and (f) feature $V_{\mathrm{con}} < 0$ because each of these two patterns has a minimum in the center of the image. The other four patterns have centered maxima corresponding to $V_{\mathrm{con}} \geq 0$. Calibration of detector positions $x_{1,2} = 0$ is performed via measurements of the coincidence count rate without double slit. Patterns (b) and (f) correspond to two-photon states on the lower hemisphere of the two-qubit Bloch sphere in Fig. 2.

Patterns (c) and (f) are special because they have nonzero curvature phase $\varphi$. Such configurations can only be achieved with defocused two-photon imaging, meaning that $\Delta z \neq 0$ for crystal imaging or $s \neq 0$ for far-field imaging. The characterizing feature of defocusing is the emergence of a checkerboardlike pattern. This changes the topology of the interference pattern by splitting the dark curves of zero coincidences into patches of low coincidence counts. A checkerboardlike pattern reduces the conditional one-photon visibility so that the two-photon state is brought closer to the horizontal equator of the two-qubit Bloch sphere.

The degree of entanglement is directly related to the conditional one-photon visibility via Eq. (26). Maximum entanglement manifests itself as $V_{\mathrm{con}} = 0$ and a total absence of separability of the interference pattern in horizontal and vertical directions. Patterns (a) and (d), on one hand, correspond to maximally entangled states as these have zero conditional one-photon visibility. Pattern (e), on the other hand, corresponds to an almost nonentangled two-photon state as the pattern almost factorizes.

The curvature phase is highly relevant for the degree of entanglement. Pattern (c), for example, has $V_{12} = -0.14 \pm 0.01$ which is rather close to zero, and, at the same time, it is strongly entangled with a concurrence of $C = 0.906 \pm 0.008$. Such combination is only possible if the curvature phase is nonzero. The curvature phase is $|\varphi| = (64.7 \pm 1.0)°$ for pattern (c). The entanglement has almost fully "migrated" from the modulus to the phase of the two-photon field profile right behind the double slit [33].

### C. Crystal imaging at $\varphi = 0$

This section presents the experimental results obtained with the crystal imaging scheme of Fig. 3(a) with zero defocus $\Delta z = 0$. We only vary the reduced slit separation $2d/M$, where $M$ is the magnification of the imaging system. Working at zero defocus, we expect to engineer two-photon states with zero curvature phase $\varphi = 0$. Figure 6 depicts the measured visibilities $V_{12}$, $V_{\mathrm{con}}$, and $V_{\mathrm{unc}}$ versus the reduced slit separation. The vertical error bars are based on the internal errors and scan resolutions of the two-photon interference patterns. The theoretical curves for $V_{12}$ and $V_{\mathrm{con}}$ are based on Eqs. (24), (25), and (14). The theoretical curve for $V_{\mathrm{unc}}$ is a plot of Eq. (33). We observe good agreement between experiment and theory.

The three plots in Fig. 6 contain a wealth of information. First of all, the shape of each curve is directly related to the phase-matching profile of the periodically poled crystal. Our theoretical curves are based on the sinc-shaped phase-matching profile in momentum representation [see Eq. (9)]. The observed agreement between experiment and theory means that the phase-matching profile is indeed sinc shaped in its momentum representation. Second, we observe that $V_{\mathrm{con}}$ and $V_{\mathrm{unc}}$ are negative for some values of the reduced slit separation. Negativity of these parameters means that we observe minima instead of maxima in the centers of the measured interference patterns. Finally, we observe that $V_{\mathrm{con}}$ and $V_{\mathrm{unc}}$ are different from each other. For the crystal imaging scheme, there is no one-to-one duality relation between these visibilities like there is for the far-field imaging scheme [see Eq. (36)]. Interestingly, the experiments prove that $V_{\mathrm{unc}}$ can be zero, while the two-photon state behind the double slit is not maximally entangled for the same geometry ($V_{\mathrm{con}} \neq 0$).

Closer inspection of Fig. 6 indicates that the majority of the measurements seem to be slightly on the right-hand side of the theoretical curves. We do not know the origin of this systematic error for certain, but a suspicious parameter

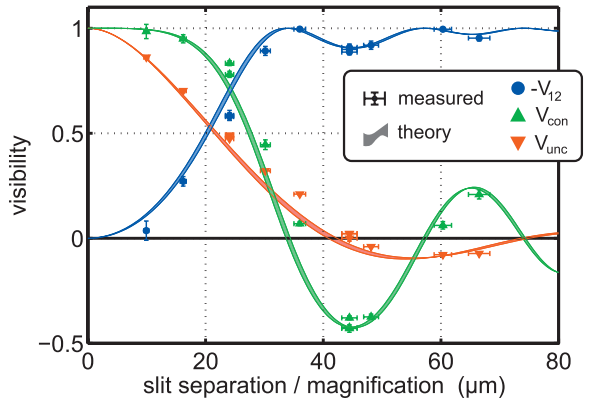


FIG. 6. (Color) Measured visibilities obtained with the crystal imaging scheme of Fig. 3(a) at $\Delta z=0$ for various reduced slit separations $2d/M$. The theoretical two-photon visibilities $V_{12}$ and $V_{\mathrm{con}}$ are calculated via Eqs. (24) and (25) for the two-photon state with engineering parameter $p$ from Eq. (14). The theoretical curve for the unconditional one-photon visibility $V_{\mathrm{unc}}$ is calculated via Eq. (33). The uncertainty in the theoretical curves, indicated by finite curve widths, originates from the uncertainty in the phase mismatch $\phi_0=0.33\pm0.05$. No fit parameters are used for the theoretical curves.

is the phase mismatch $\phi_0$. It was determined to be $\phi_0=0.33\pm0.05$ from measurements of the SPDC spectrum. However, if we would plot the theoretical visibilities using $\phi_0=0.65$ we would observe excellent agreement between theory and measured visibilities. This means that a systematic error of only 0.3 °C in the phase-matching temperature would already explain the observed small systematic difference between experiment and theory.

In Fig. 7 the engineered two-photon states are depicted as points in a square with $V_{12}$ and $V_{\mathrm{con}}$ along the axes. The points on the left half plane correspond to the measurements from the crystal imaging scheme. The measurements are in excellent agreement with the complementarity relation $V_{12}^2+V_{\mathrm{con}}^2=1$ that is predicted for two-photon states with zero curvature phase $\varphi=0$.

Previously, of the two-photon states with $V_{12}<0$, only the fully paired two-photon state had been prepared by positioning a double slit with large slit separation very close to the crystal [9,27,32]. We now demonstrate that the fully paired two-photon state can also be prepared by imaging the two-photon source onto a double slit. To the best of our knowledge, two-photon states corresponding to $-1<V_{12}<0$ or $V_{\mathrm{con}}<0$ have never been prepared before. Our experiments with the crystal imaging scheme are phase-sensitive measurements of the two-photon field structure in an image plane of the crystal center.

### D. Far-field imaging at $\varphi=0$

We present the experimental results obtained with the far-field imaging scheme of Fig. 3(b) with zero defocus ($s=0$), where we expect to engineer two-photon states with zero curvature phase $\varphi=0$. We only vary the relative slit separation $2d/(2f_2\theta_d)$, where $2f_2\theta_d$ is the diameter of the pump beam in the double-slit plane. Figure 8 depicts the measured

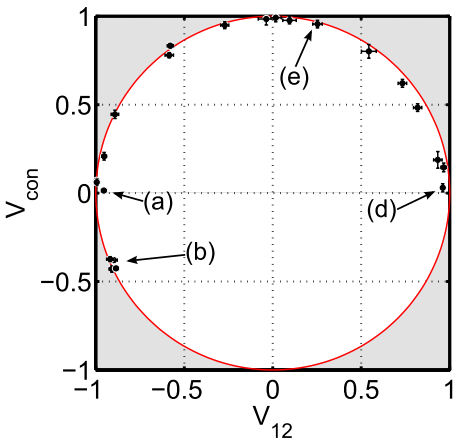


FIG. 7. (Color online) Measured visibilities of engineered two-photon states with zero curvature phase $\varphi=0$. The two-photon states on the left side are prepared with the crystal imaging scheme in Fig. 4(a) at $\Delta z=0$. The two-photon states on the right are prepared with the far-field imaging scheme in Fig. 4(b) at $s=0$. The annotated measurements correspond to fringe patterns in Fig. 5. The exterior of the circle is forbidden by the complementarity relation $V_{\mathrm{con}}^2+V_{12}^2\leq1$. Figure 2 graphically indicates how $V_{\mathrm{con}}$ and $V_{12}$ relate to the engineered two-photon state.

visibilities $V_{12}$, $V_{\mathrm{con}}$, and $V_{\mathrm{unc}}$ versus the relative slit separation. The horizontal error bars are determined by the 10% uncertainty in the pump divergence. The vertical error bars are based on the internal error and scan resolution of the two-photon interference patterns. The theoretical curves for $V_{12}$ and $V_{\mathrm{con}}$ are based on Eqs. (24), (25), and (18). The theoretical curve for $V_{\mathrm{unc}}$ is a plot of Eq. (34).

We observe excellent agreement between theory and the measured visibilities. For small slit separations we observe that the two-photon visibility difference $V_{12}\approx0$, meaning that the moduli of the paths of the two photons are hardly correlated. We also observe that these states are approximately nonentangled because $V_{\mathrm{con}}\approx1$. For larger slit separations $V_{12}$ approaches 1, indicating that the concurrence

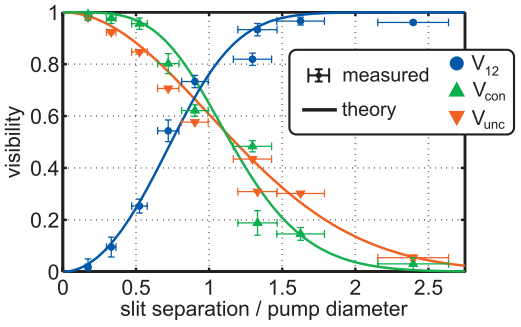


FIG. 8. (Color) Measured visibilities obtained with the far-field imaging scheme of Fig. 3(b) at $s=0$ for various configurations of the slit separation $2d$ relative to the Gaussian pump diameter in the double-slit plane $2f_2\theta_p$. The theoretical two-photon visibilities $V_{12}$ and $V_{\mathrm{con}}$ are calculated via Eqs. (24) and (25) for the two-photon state with engineering parameter $p$ from Eq. (18). The expected curve for the unconditional one-photon visibility $V_{\mathrm{unc}}$ is calculated via Eq. (34). No fit parameters are used for the theoretical curves.

increases, and $V_{\mathrm{con}}$ goes down. Furthermore, we observe that the conditional and the unconditional one-photon visibilities are different from each other. Interesting is the observation that the curves for $V_{\mathrm{con}}$ and $V_{\mathrm{unc}}$ cross each other. This crossing has neither been predicted nor observed before. It is in agreement with the duality relation of Eq. (36).

Each engineered two-photon state can be depicted as a point in a square with $V_{12}$ and $V_{\mathrm{con}}$ along the axes. This representation is visualized in Fig. 7, where the points on the right half plane correspond to our measurements from the far-field imaging scheme. The measurements are in excellent agreement with the complementarity relation $V_{12}^2+V_{\mathrm{con}}^2=1$ that is predicted for two-photon states with zero curvature phase $\varphi=0$. Previously, an experimental demonstration of complementarity was performed by Abouraddy *et al.* [13], albeit with less accuracy.

### E. Crystal imaging at nonzero curvature phase

Two-photon states with nonzero curvature phase have been engineered with the crystal imaging scheme in Fig. 3(a) at nonzero defocus distance $\Delta z \neq 0$. A plane slightly behind the crystal center is imaged onto the double slit. Due to the propagation away from the crystal-center plane, the phase-matching profile $\xi_z(z;\Delta z)$ has developed a certain wave-front curvature. This wave-front curvature causes the curvature phase $\varphi$ to become nonzero. The curvature phase is highly relevant for the two-photon interference pattern behind the double slit. The characterizing feature of two-photon states with $0<|\varphi|<\pi$ is that $V_{12}^2+V_{\mathrm{con}}^2<1$, implying that these states are located in the interior of the complementarity circle. The curvature phase is also relevant for the degree of entanglement.

Figure 9 shows the two-photon visibilities $V_{12}$ and $V_{\mathrm{con}}$ of eight two-photon states that are engineered with the crystal imaging scheme at increasing defocus distance $\Delta z$. For this series, we have used a reduced slit separation of $2d/M=(44.5\pm1.3)$ $\mu$m and eight equidistant values of $\Delta z$. We observe that the two-photon state at $\Delta z \approx 0$ has approximately zero curvature phase, as this measurement lies on the complementarity circle $V_{12}^2+V_{\mathrm{con}}^2=1$. For increasing defocus, we observe that the two-photon states obtain nonzero curvature phases, as their two-photon visibilities lie in the interior of the complementarity circle.

The theoretical curve, including its uncertainty region, is calculated from the engineering parameter $p$ given by Eq. (14). The visibilities $V_{12}$ and $V_{\mathrm{con}}$ are then derived via Eqs. (24) and (25). The wiggly nature of the theoretical curve in Fig. 9 originates from the Fresnel-type integrals in the equation for $p$. We observe reasonable agreement between theory and experiment. All the more so, a strong resemblance is found when considering the relative orientation of two points within any pair of successive measurement points. This resemblance is striking because these relative orientations are quite erratic while the defocus distance $\Delta z$ is increased over equidistant values.

The measurements in Fig. 9 are the first phase-sensitive measurements of the two-photon field structure in an image of a plane close to the crystal center, i.e., within the Rayleigh range of the phase-matching profile $\xi_z(x;z)$.

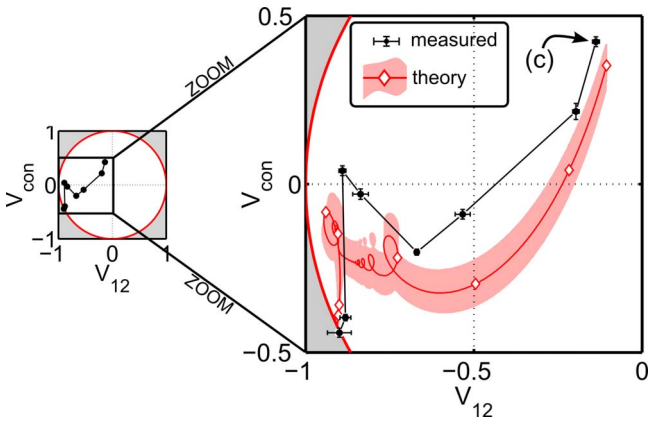


FIG. 9. (Color online) Measured visibilities of two-photon states engineered with the crystal imaging scheme of Fig. 3(a) at increasing defocus $\Delta z$. The series contains measurements at eight equidistant displacements of the cylinder lens ranging from $\Delta z=-(0.20\pm0.04)$ mm to $\Delta z=(3.30\pm0.04)$ mm at the annotated measurement (c). The theoretical curve is calculated via Eqs. (24) and (25) with engineering parameter $p$ from Eq. (14). The points on the theoretical curve (diamonds) relate to the measured points in the indicated order. The uncertainty of the theoretical curve originates from the phase mismatch $\Delta\phi_0=0.33\pm0.05$ and a $\pm3\%$ uncertainty in the reduced slit separation $2d/M$. The annotated measurement corresponds to fringe pattern (c) in Fig. 5.

### F. Far-field imaging at nonzero curvature phase

Two-photon states with nonzero curvature phase have also been engineered with the far-field imaging scheme in Fig. 3(b) at $s \neq 0$. The phase front of the pump beam in the double-slit plane is curved now because the pump waist is located in front of the nonlinear crystal. The wave-front curvature of the pump beam in the double-slit plane causes the curvature phase $\varphi$ to become nonzero. States with nonzero curvature phase have $V_{12}^2+V_{\mathrm{con}}^2<1$ implying that such states are located in the interior of the complementarity circle. The curvature phase is relevant for the two-photon interference pattern as well as the degree of entanglement.

Figure 10 shows the two-photon visibilities $V_{12}$ and $V_{\mathrm{con}}$ of six two-photon states that are engineered with the far-field imaging scheme with $s \neq 0$. We observe that the two-photon state behind the double slit has nonzero curvature phase as the states lie inside the complementarity circle. We also demonstrate that it is possible to reach the lower hemisphere of the two-qubit Bloch sphere ($V_{\mathrm{con}}<0$ in Fig. 2) by altering the pump beam. Two-photon states on the lower hemisphere have never been prepared before.

## VI. CONCLUSION

This paper demonstrates the engineering and characterization of spatially entangled two-photon states behind a double slit that is symmetrically illuminated with a pure two-photon state. Engineering is achieved by tailoring the optical imaging system in between the two-photon source and the double slit. We have discussed a crystal imaging scheme where the two-photon source itself is imaged onto the double slit. The curvature phase $\varphi$ has also been discussed, and it is shown

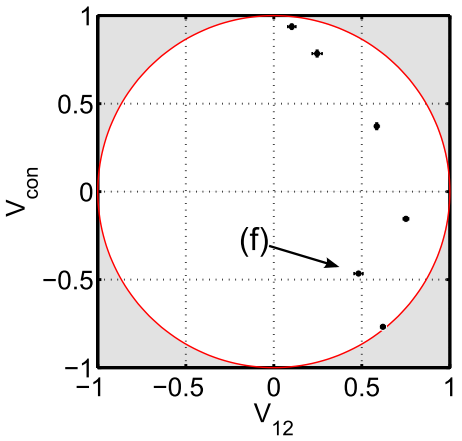


FIG. 10. (Color online) Measured visibilities of two-photon states engineered with the far-field imaging scheme of Fig. 3(b) at pump beam defocus $s \neq 0$. The annotated measurement corresponds to fringe pattern (f) in Fig. 5.

that $\varphi$ is highly relevant for the two-photon interference pattern as well as the degree of entanglement behind the double slit. State characterization is achieved by performing measurements of the complete two-photon interference pattern in the far field of the double slit.

The presented analysis of two-photon state engineering is complete for illumination systems within the following three restrictions. First, we consider illumination schemes and double slits that obey mirror symmetry around the optical axis (see Sec. II A). Second, we assume slits that are narrower than the transverse coherence width of the illumination (see Sec. II B). Third, the two-photon source is based on any type of SPDC in a periodically poled crystal or type-I SPDC in a uniform crystal provided that the transverse walk-off of the pump beam is negligible with respect to its width (see Sec. II C and Appendix).

For a symmetric setup and narrow slits, the two-photon state behind the double slit becomes a coherent superposition of a paired state, where the photons emerge form the same slit, and an antipaired state, where the photons appear from opposite slits. The relative phase between both contributions is the curvature phase $\varphi$. The absolute balance between the paired and antipaired components is described by state parameter $\alpha$.

It is demonstrated how to engineer any two-photon state in this form. The paired two-photon component dominates if the crystal imaging scheme is used. The antipaired two-photon component dominates if the far field of the source is imaged onto the double slit. The precise balance between the paired and antipaired components is controlled by tailoring the magnification properties of these imaging systems. The curvature phase $\varphi$ is fully controlled by utilizing the phase-front curvatures of the pump profile $E_{p,z}(x;z)$ and phase-matching profile $\xi_z(x;z)$. The phase-matching profile governs the engineered two-photon state in the crystal imaging scheme. The pump profile governs the engineered two-photon state in the far-field imaging scheme.

We have shown that the two-photon interference pattern in the far field of the double slit serves as a fingerprint of the engineered two-photon state. The pattern directly yields the one-photon visibility $V_{\mathrm{con}}$ and the two-photon visibility difference $V_{12}$. These visibilities conveniently relate to the position on the two-qubit Bloch sphere that we have presented to graphically depict any engineered two-photon state. This sphere is also highly convenient to read off the concurrence.

We have engineered and characterized more than 30 different two-photon states. Good agreement between measurements and theory is observed. Two-photon states exhibiting strong curvature phase, states with $V_{\mathrm{con}} < 0$, and states with $-1 < V_{12} < 0$ have never been prepared before. Our experiments with the crystal imaging scheme are phase-sensitive measurements of the two-photon field structure in an image of a plane close to the crystal center, i.e., within the Rayleigh range of the phase-matching profile $\xi_z(x;z)$.

Using the crystal imaging scheme, we have presented measurements of the unconditional one-photon visibility $V_{\mathrm{unc}}$ in an image plane of the crystal center. In the far-field imaging scheme, we have demonstrated the duality between $V_{\mathrm{con}}$ and $V_{\mathrm{unc}}$ for Gaussian pump profile that is loosely focused in the crystal-center plane. The experimental results are in agreement with theory.

## VII. DISCUSSION: TUNING IN HIGH-DIMENSIONAL HILBERT SPACE

In this paper, the tuning range of the engineered two-photon states has been restricted to a two-dimensional Hilbert space spanned by two out of four maximally entangled Bell states [see Eq. (4)]. However, spatially entangled two-photon states generated via SPDC allow for tuning in much higher-dimensional Hilbert space. We will now discuss some experimental tuning parameters that remained untouched in this paper.

The entire four-dimensional Hilbert space of Eq. (3) becomes accessible if one allows asymmetric illumination schemes with distinguishable photons. The coefficients $c_1$ and $c_4$ become uncoupled by allowing asymmetric illumination schemes. Such asymmetry could be achieved by applying an asymmetric pump profile or by moving the double slit transversely to a noncentered position. The coefficients $c_2$ and $c_3$ become uncoupled if one uses distinguishable photons in combination with an asymmetric illumination scheme. Distinguishable spatially entangled photons can be produced via type-II SPDC in a periodically poled crystal [7,24,27] or by using two double-slit apertures positioned in the two output ports of a beam splitter. An experiment where $c_2 = -c_3$ has been demonstrated in Ref. [24] by placing birefringent crystals in front of the double slit.

One can also turn to multidimensionally entangled two-photon states by using multislit apertures [29–32]. To tune between different multidimensionally entangled states, one could use a variable pump profile based on a spatial light modulator. Another interesting tuning parameter is the temperature-dependent phase mismatch $\phi_0$ of the periodically poled crystal. The analysis in this paper may serve as a good starting point to make the extension to quantum state engineering of multidimensionally entangled two-photon states.

## ACKNOWLEDGMENTS

We acknowledge stimulating discussions with J. P. Woerdman, D. Bouwmeester, and E. F. C. Driessen. The research is supported by the Stichting voor Fundamenteel Onderzoek der Materie (FOM).


## APPENDIX: VALIDITY OF VARIOUS PHASE-MATCHING GEOMETRIES

The theoretical analysis in this paper is based on noncritical type-I phase matching (see Sec. II C). In this Appendix, however, we show that the analysis also applies to noncritical type-II as well as critical type-I phase matching. Noncritical phase matching is generally applied in quasi-phase-matched processes, and critical phase matching is generally applied in uniform crystals.

We will first give expressions for the two-photon field profile in the crystal-center plane for various phase-matching geometries. We consider a nonlinear crystal with two parallel planar facets in transverse $xy$ planes. For the critically phase-matched cases treated below, the crystallographic optical axis lies in the positive $yz$ plane. Following Refs. [36] and [45] we use a generic quasimonochromatic expression for the two-photon field profile in the crystal-center plane.

$$\tilde{A}_{\mathrm{crys}}(\mathbf{q}_1,\mathbf{q}_2) \propto \tilde{E}_p(\mathbf{q}_1+\mathbf{q}_2)\mathrm{sinc}\left[\tfrac{1}{2}L\Delta k_z(\mathbf{q}_1,\mathbf{q}_2)\right], \quad (41)$$

where $\mathrm{sinc}(x) \equiv \sin(x)/x$, and the wave-vector mismatch

$$\Delta k_z(\mathbf{q}_1,\mathbf{q}_2) = k_z(\mathbf{q}_1+\mathbf{q}_2,\omega_p,\sigma_p) - k_z(\mathbf{q}_1,\omega_0,\sigma_1) - k_z(\mathbf{q}_2,\omega_0,\sigma_2) - (2\pi\Lambda^{-1}), \quad (42)$$

where $k_z(\mathbf{q},\omega,\sigma)$ is the $z$ component of the wave vector of a plane wave with transverse wave vector $\mathbf{q}$, radial frequency $\omega$, and polarization $\sigma$. The fourth term between parentheses does not apply to uniform crystals; it only applies to periodically poled crystals where $\Lambda$ is the poling period. All other symbols are defined in Sec. II C of the main text. Equation (41) is valid for any type of phase matching as it is based on a simple plane-wave expansion. The Taylor expansion of Eq. (42) up to second-order becomes approximately

$$\Delta k_z(\mathbf{q}_1,\mathbf{q}_2) \approx C + \frac{|\mathbf{q}_-|^2}{4n_0\omega_0/c} + \begin{cases} 0 & \text{for noncritical type I and type II} \\ -\rho[\mathbf{q}_+]_y & \text{for critical type I } (e \to oo) \\ +\tfrac{1}{2}\rho[\mathbf{q}_+ - \mathbf{q}_-]_y & \text{for critical type II } (o \to oe), \end{cases} \quad (43)$$

where $C$ is the wave-vector mismatch in the forward direction, $\mathbf{q}_\pm \equiv \mathbf{q}_1 \pm \mathbf{q}_2$, $n_0$ is the refractive index at the down-converted frequency, and $\rho$ is the walk-off angle for extraordinary-polarized light ($\rho > 0$ if directed away from the crystallographic optical axis). We have omitted the relatively small direction, frequency, and polarization dependencies of the refractive index in all second-order terms. We have also omitted the frequency dependence of the walk-off angle $\rho$.

In the noncritically phase-matched case, above equations directly lead to Eqs. (8) and (9) describing the generated two-photon field profile in the main text of this paper. We therefore conclude that the analysis in this paper applies to all noncritically phase-matched SPDC processes. For noncritical type-II phase matching, one can easily add the polarization dependence of the refractive to the phase-matching profile in Eq. (9) of the main text by substituting $n_0$ for $2n_1n_2/(n_1+n_2)$, where $n_1$ and $n_2$ are the refractive indices of the two down-converted photons.

For critical type-I phase matching, a linear term appears in the wave-vector mismatch in Eq. (43). This linear term can be neglected if the pump beam is sufficiently loosely focused; loose focusing causes the momentum representation $\tilde{E}_p(\mathbf{q}_+)$ to become compact such that it over-rules the much broader $\mathbf{q}_+$ dependence of $\Delta k_z$ in Eq. (41). This criterion is met if the walk-off term $\frac{1}{2}L\rho[\mathbf{q}_+]_y$ in the argument of the sinc function is much smaller than a radian at a typical value of $[\mathbf{q}_+]_y = 2/w_p$, where $w_p$ is the width of the Gaussian pump beam in real space and $2/w_p$ is the width of the pump beam in transverse momentum space. The loose-focusing criterion thus becomes $L\rho \ll w_p$ for critical type-I phase matching, simply stating that the transverse walk-off distance $L\rho$ must be much smaller than the pump beam width. In Sec. II C, we have already assumed loose focusing (Rayleigh range pump $\gg$ crystal length) in order to obtain simple expressions for the engineering parameters in Eqs. (14) and (18). The loose-focusing criterion $L\rho \ll w_p$ for critical type-I phase matching is generally stronger.

For critical type-II phase matching, the linear term *cannot* be screened by loose focusing. It is immediately clear from Eq. (43) that the linear term in $[\mathbf{q}_-]_y$ affects Eq. (41) even if the momentum representation $\tilde{E}_p(\mathbf{q}_+)$ is very compact. It is therefore generally not correct to use Eqs. (8) and (9) for critical type-II SPDC. Note, however, that even in this critical type-II case, our engineering description remains valid if the slits are oriented in the $y$ direction; the linear walk-off term $[\mathbf{q}_-]_y$ becomes irrelevant if the transverse walk-off is directed along the orientation of the slits.

[1] T. B. Pittman, D. V. Strekalov, D. N. Klyshko, M. H. Rubin, A. V. Sergienko, and Y. H. Shih, Phys. Rev. A **53**, 2804 (1996).
[2] Y. Shih, Rep. Prog. Phys. **66**, 1009 (2003).
[3] R. Ghosh and L. Mandel, Phys. Rev. Lett. **59**, 1903 (1987).
[4] P. H. Souto Ribeiro, C. H. Monken, and G. A. Barbosa, Appl. Opt. **33**, 352 (1994).
[5] D. N. Klyshko, Sov. Phys. JETP **67**, 1131 (1988).
[6] D. V. Strekalov, A. V. Sergienko, D. N. Klyshko, and Y. H. Shih, Phys. Rev. Lett. **74**, 3600 (1995).
[7] A. Gatti, E. Brambilla, and L. A. Lugiato, Phys. Rev. Lett. **90**, 133603 (2003).
[8] A. N. Boto, P. Kok, D. S. Abrams, S. L. Braunstein, C. P. Williams, and J. P. Dowling, Phys. Rev. Lett. **85**, 2733 (2000).
[9] M. D'Angelo, M. V. Chekhova, and Y. Shih, Phys. Rev. Lett. **87**, 013602 (2001).
[10] A. Mair, A. Vaziri, G. Weihs, and A. Zeilinger, Nature (London) **412**, 313 (2001).
[11] W. H. Peeters, E. J. K. Verstegen, and M. P. van Exter, Phys. Rev. A **76**, 042302 (2007).
[12] T. G. Noh and C. K. Hong, J. Korean Phys. Soc. **33**, 383 (1998).
[13] A. F. Abouraddy, M. B. Nasr, B. E. A. Saleh, A. V. Sergienko, and M. C. Teich, Phys. Rev. A **63**, 063803 (2001).
[14] E. J. S. Fonseca, J. C. Machado da Silva, C. H. Monken, and S. Pádua, Phys. Rev. A **61**, 023801 (2000).
[15] B. E. A. Saleh, A. F. Abouraddy, A. V. Sergienko, and M. C. Teich, Phys. Rev. A **62**, 043816 (2000).
[16] E. J. S. Fonseca, C. H. Monken, S. Pádua, and G. A. Barbosa, Phys. Rev. A **59**, 1608 (1999).
[17] M. D'Angelo, Y.-H. Kim, S. P. Kulik, and Y. Shih, Phys. Rev. Lett. **92**, 233601 (2004).
[18] R. S. Bennink, S. J. Bentley, R. W. Boyd, and J. C. Howell, Phys. Rev. Lett. **92**, 033601 (2004).
[19] A. F. Abouraddy, T. Yarnall, B. E. A. Saleh, and M. C. Teich, Phys. Rev. A **75**, 052114 (2007).
[20] T. Yarnall, A. F. Abouraddy, B. E. A. Saleh, and M. C. Teich, Phys. Rev. Lett. **99**, 170408 (2007).
[21] C. K. Law and J. H. Eberly, Phys. Rev. Lett. **92**, 127903 (2004).
[22] E. J. S. Fonseca, C. H. Monken, and S. Pádua, Phys. Rev. Lett. **82**, 2868 (1999).
[23] C. K. Hong and T. G. Noh, J. Opt. Soc. Am. B **15**, 1192 (1998).
[24] W. A. T. Nogueira, S. P. Walborn, S. Pádua, and C. H. Monken, Phys. Rev. Lett. **86**, 4009 (2001).
[25] G. Lima, F. A. Torres-Ruiz, L. Neves, A. Delgado, C. Saavedra, and S. Pádua, J. Phys.: Conf. Ser. **84**, 012012 (2007).
[26] L. Neves, G. Lima, E. J. S. Fonseca, L. Davidovich, and S. Pádua, Phys. Rev. A **76**, 032314 (2007).
[27] R. Shimizu, T. Yamaguchi, Y. Mitsumori, H. Kosaka, and K. Edamatsu, Phys. Rev. A **77**, 032338 (2008).
[28] G. Taguchi, T. Dougakiuchi, N. Yoshimoto, K. Kasai, M. Iinuma, H. F. Hofmann, and Y. Kadoya, Phys. Rev. A **78**, 012307 (2008).
[29] L. Neves, S. Pádua, and C. Saavedra, Phys. Rev. A **69**, 042305 (2004).
[30] L. Neves, G. Lima, J. G. Aguirre Gómez, C. H. Monken, C. Saavedra, and S. Pádua, Phys. Rev. Lett. **94**, 100501 (2005).
[31] G. Lima, L. Neves, I. F. Santos, J. G. Aguirre Gómez, C. Saavedra, and S. Pádua, Phys. Rev. A **73**, 032340 (2006).
[32] R. Shimizu, K. Edamatsu, and T. Itoh, Phys. Rev. A **74**, 013801 (2006).
[33] K. W. Chan, J. P. Torres, and J. H. Eberly, Phys. Rev. A **75**, 050101(R) (2007).
[34] S. Hill and W. K. Wootters, Phys. Rev. Lett. **78**, 5022 (1997).
[35] A. F. Abouraddy, B. E. A. Saleh, A. V. Sergienko, and M. C. Teich, Phys. Rev. A **64**, 050101(R) (2001).
[36] C. H. Monken, P. H. Souto Ribeiro, and S. Pádua, Phys. Rev. A **57**, 3123 (1998).
[37] A. E. Siegman, *Lasers*, 1st ed. (University Science Books, California, 1986), Chap. 20, Eq. (14).
[38] J. C. Howell, R. S. Bennink, S. J. Bentley, and R. W. Boyd, Phys. Rev. Lett. **92**, 210403 (2004).
[39] A. Ekert and P. L. Knight, Am. J. Phys. **63**, 415 (1995).
[40] G. Jaeger, M. A. Horne, and A. Shimony, Phys. Rev. A **48**, 1023 (1993).
[41] G. Jaeger, A. Shimony, and L. Vaidman, Phys. Rev. A **51**, 54 (1995).
[42] D. F. Walls, Am. J. Phys. **45**, 952 (1977).
[43] D. Z. Cao, Z. Li, Y. H. Zhai, and K. Wang, Eur. Phys. J. D **33**, 137 (2005).
[44] W. H. Peeters and M. P. van Exter, Opt. Express **16**, 7344 (2008).
[45] M. M. Fejer, G. A. Magel, D. H. Jundt, and R. L. Byer, IEEE J. Quantum Electron. **28**, 2631 (1992).